Journal of Applied Mechanics Vol.13, pp.769-780 (August 2010) JSCE

Numerical simulation of flow at an open-channel confluence using depth-averaged 2D models with effects of secondary currents

Mung Dinh Thanh*, Ichiro Kimura**, Yasuyuki Shimizu*** and Takashi Hosoda****

* Student Member of JSCE, Graduate Student, Hydraulic Research Laboratory, Hokkaido University
(Sapporo 060-8628, Kita-ku, Kita-13, Nishi-8,Japan)
**Member of JSCE, Dr. of Eng., Associate Professor, Hydraulic Research Laboratory, Hokkaido University
(Sapporo 060-8628, Kita-ku, Kita-13, Nishi-8,Japan)
***Member of JSCE, Dr. of Eng., Professor, Hydraulic Research Laboratory, Hokkaido University
(Sapporo 060-8628, Kita-ku, Kita-13, Nishi-8, Japan)
****Member of JSCE, Dr. of Eng., Professor, Department of Urban Management, Kyoto University
(Kyoto-Daigaku Katsura, Nishikyo-ku, Kyoto 615-8530, Japan)

Open-channel confluences are common in nature as well as in hydraulic structures and play an important role in fluvial channel processes. Flow at these regions is characterized by three dimensionality and is strongly affected by secondary currents induced by channel streamline curvature. A 3D model enables to describe and compute most characteristics of flow in this region. However, such a model is costly and is not practical. Therefore, it should be useful and more practical, if simpler models are developed. For this purpose, we introduce some of such models, depth-averaged 2D models. In the present study, first, selection of a suitable turbulence model is done. Then, four different types of depth-averaged 2D models are performed. Computed results with these models are also compared to the experimental ones and to each other for discussion about adequacies of these models.

Key Words: *Open channel flow, secondary current, depth-averaged 2D model*

1. Introduction

Channel confluences are common in natural rivers and hydraulic structures and play an important role in fluvial channel processes. Flow features in these regions are complicated and are characterized with one separation zone or recirculation zone immediately downstream of the confluence in the inner bank side and one contracted flow region in the outer bank side. These features are influenced by numerous factors, such as geometry ones, for example the size, shape, slope of channels and angle between channels, and flow ones, for instance the Froude number in the downstream flow, the ratio of discharge in the two channels. Complexity of flow at the vicinity of the junction arises due to deflection of lateral flow entering the main channel and this makes channel streamlines in the post-junction region curved. Recent 3D studies, such as Weber et al.[1)], Huang et al.[2)], Qing-Yuan et al.[3)], show that flow in a junction are three-dimensional with predominant secondary currents of the first kind induced by curvature of the streamlines in comparison with the ones driven by turbulence. However, except for 3D computational models, normal 2D models do not usually include this flow pattern. Not considering secondary currents in modeling of these model leads to poor performance in the cases in which flow problems in the junction as well as confluence are concerned.

Moreover, using 3D computational models is always a very good approach and is encouraged to predict flow in various channels in general and in a confluence in particular. However, this work claims much labor and is expensive.

For the reasons above, depth-averaged 2D computational models considering effects of secondary currents are developed to predict flow in curved open channels. Several models of this kind proposed are ones of Kalkwijk & de Vriend[4], of Hosoda et al.[5] in which, lag between main flows and secondary currents is included, and of Onda et al.[6] with considering change of the velocity profile induced by development of secondary currents. The latter two have been recently paid attention and some studies applying these two models have been conducted. For instance, works of Kimura et al.[7] are based on applying these models to study features of flow and sediment transport in open-channel with a side cavity. One another application of these models has been carried out by Kimura et al.[8] to study flow and sediment transport in meandering channels. Good performances are obtained in their studies. However, there is no application of these models carried out to open-channel confluence flow so far.

The purpose of the present study is to apply depth-averaged 2D models with effects of secondary currents for computation of flow in a vicinity of a channel confluence. In this study, four depth-averaged 2D models applied are

(a) Model 1: a conventional 2D model using zero-equation turbulence models without effects of secondary currents;
(b) Model 2: a 2D model with effects of secondary current without consideration of lag between the streamline curvature and development of secondary currents;
(c) Model 3: a 2D model with effects of secondary currents and lag between the streamline curvature and development of secondary currents; and,
(d) Model 4: a 2D model that consider effects of secondary currents, lag between the streamline curvature and development of secondary currents as well as change of mainstream velocity profile influenced by secondary currents.

Attempts to apply Model 2 are done during the process of implementation of this study, but are not successful. The reason for this may be attributed to very sharp streamline curvature of flow downstream of the junction causing very instability of this model. Therefore, in the following, only the results obtained from the models 1, 3 and 4 are reported.

Computational results are compared to experimental results of Weber et al.1). The present computed results show evident distinctions between using the depth-average models with effects of secondary currents and using the model without this consideration for the case in which secondary currents have strong effects on flow pattern.

2. Computational models

2.1 Fundamental equations

The governing equations used in this study are depth-averaged 2D shallow water flow equations described in Kimura et al.[7] in the Cartesian coordinate as follows.

Continuity equation:

$$\frac{\partial h}{\partial t}+\frac{\partial M}{\partial x}+\frac{\partial N}{\partial y}=0 \tag{1}$$

Momentum equations:

$$\begin{aligned}\frac{\partial M}{\partial t}+\frac{\partial \beta uM}{\partial x}+\frac{\partial \beta vM}{\partial y}+gh\frac{\partial (h+z_b)}{\partial x}=\\ gh\sin\theta-\frac{\tau_{bx}}{\rho}+\frac{\partial -\overline{u'^2}h}{\partial x}+\frac{\partial -\overline{u'v'}h}{\partial y}\\ +\nu\left\{\frac{\partial}{\partial x}\left(h\frac{\partial u}{\partial x}\right)+\frac{\partial}{\partial y}\left(h\frac{\partial u}{\partial y}\right)\right\}+\hat{S}_{cx}\end{aligned} \tag{2}$$

$$\begin{aligned}\frac{\partial N}{\partial t}+\frac{\partial \beta uN}{\partial x}+\frac{\partial \beta vN}{\partial y}+gh\frac{\partial (h+z_b)}{\partial y}=\\ -\frac{\tau_{by}}{\rho}+\frac{\partial -\overline{v'u'}h}{\partial x}+\frac{\partial -\overline{v'^2}h}{\partial y}\\ +\nu\left\{\frac{\partial}{\partial x}\left(h\frac{\partial v}{\partial x}\right)+\frac{\partial}{\partial y}\left(h\frac{\partial v}{\partial y}\right)\right\}+\hat{S}_{cy}\end{aligned} \tag{3}$$

where (x, y): spatial coordinate, (u, v): depth-averaged velocity components in (x, y) directions, t: time, h: water depth, (M, N): discharge fluxes in (x, y) directions defined as (hu, hv) respectively, g: gravity acceleration, (u’, v’): turbulence velocities in (x, y) directions, z_b: bed level, (τ_{bx}, τ_{by}): bottom shear stress vectors, ν: dynamic viscosity coefficient, sinθ: bed slope, ρ: water density, β: momentum coefficient, $-\overline{u'^2}, -\overline{u'v'}, -\overline{v'^2}$: depth-averaged Reynolds stress tensors, and $\hat{S}_{cx}$, $\hat{S}_{cy}$: additional terms caused by secondary currents and defined later.

Components of the bottom shear stress vector are evaluated as

$$\tau_{bx}=\frac{f\rho u}{2}\sqrt{u^2+v^2};\quad \tau_{by}=\frac{f\rho v}{2}\sqrt{u^2+v^2} \tag{4}$$

in which, f: friction factor being a function of local Reynolds, $R_e' \equiv uh/\nu$, evaluated as follows.

$$f=\frac{6}{R_e'}\quad \text{for } R_e' \le 430 \tag{5a}$$

$$\sqrt{\frac{2}{f}}=A_S-\frac{1}{\kappa}\left[1-\ln\left(R_e'-\sqrt{\frac{2}{f}}\right)\right]\text{for } R_e' \ge 430 \tag{5b}$$

where κ = 0.41, A_S = 5.5.

The depth-averaged Reynolds stress tensors are evaluated based on the 0-equation turbulence model. For linear model, this term is evaluated as

$$-\overline{u_i u_j} = (D_h + \nu) S_{ij} - \frac{2}{3} k \delta_{ij} \tag{6}$$

but for nonlinear one, a non-linear term is added to the Reynolds stress tensor proposed by Kimura et al.[9] as

$$\begin{aligned} -\overline{u_i u_j} &= (D_h + \nu) S_{ij} - \frac{2}{3} k \delta_{ij} \\ &- \lambda_p \frac{h}{u_*} D_h \sum_{\beta=1}^{3} c_\beta \left(S_{\beta ij} - \frac{1}{3} S_{\beta\alpha\alpha} \delta_{ij} \right) + C_{ij} u_*^2 \end{aligned} \tag{7}$$

$i, j = 1,2$

Here, $S_{\beta ij}$ is defined as

$$S_{1ij} = \frac{\partial U_i}{\partial x_\gamma} \frac{\partial U_j}{\partial x_\gamma} \tag{8a}$$

$$S_{2ij} = \frac{1}{2} \left(\frac{\partial U_\gamma}{\partial x_i} \frac{\partial U_j}{\partial x_\gamma} + \frac{\partial U_\gamma}{\partial x_j} \frac{\partial U_i}{\partial x_\gamma} \right) \tag{8b}$$

$$S_{3ij} = \frac{\partial U_\gamma}{\partial x_i} \frac{\partial U_\gamma}{\partial x_j} \tag{8c}$$

D_h is eddy viscosity and is evaluated based on an 0-equation turbulence model with considering reduction of eddy viscosity near wall . In Eq. (6), D_h is evaluated

$$D_h = f_D \alpha h u_* \tag{9}$$

while D_h in Eq.(7) considers contribution of strain and spin and is evaluated as

$$D_h = f_D c_D \alpha h u_* \tag{10}$$

k is depth-averaged turbulent kinetic energy evaluated by the empirical formula proposed by Nezu & Nakagawa[10] as

$$k = 2.07 u_*^2 \tag{11}$$

Here, u_* is local friction velocity ($\equiv \sqrt{f(u^2 + v^2)}$); α is calibrated constant ($\alpha = 0.80$ is used in this study).

λ_p is a coefficient calculated using the approach of Kimura et al.[9] ($\lambda_p = 4.29$ in the present study).

f_D is an eddy viscosity dumping function and is evaluated as

$$f_D = 4 \frac{y_w}{h} \left(1 - \frac{y_w}{h} \right) \quad \text{for} \quad y_w \le \frac{h}{2} \tag{12a}$$

$$f_D = 1 \quad \text{for} \quad y_w > \frac{h}{2} \tag{12b}$$

Here, y_w is wall distance and h is water depth.

c_D is the coefficient of eddy viscosity and is a function of strain and rotation parameters as follows

$$c_D = \frac{1 + c_{ns} S^2 + c_{n\Omega} \Omega^2}{1 + c_{ds} S^2 + c_{d\Omega} \Omega^2 + c_{ds\Omega} S \Omega + c_{ds1} S^4 + c_{d\Omega 1} \Omega^4 + c_{ds\Omega 1} S^2 \Omega^2} \tag{13}$$

Here, S and Ω are strain and rotation parameters, respectively and defined as

$$S = \lambda_p \frac{h}{u_*} \sqrt{\frac{1}{2} S_{ij} S_{ij}}, \quad \Omega = \lambda_p \frac{h}{u_*} \sqrt{\frac{1}{2} \Omega_{ij} \Omega_{ij}} \tag{14}$$

$$S_{ij} = \frac{\partial U_i}{\partial x_j} + \frac{\partial U_j}{\partial x_i}, \quad \Omega_{ij} = \frac{\partial U_i}{\partial x_j} - \frac{\partial U_j}{\partial x_i} \tag{15}$$

c_{ns}, $c_{n\Omega}$, c_{ds}, $c_{d\Omega}$, $c_{ds\Omega}$, c_{ds1}, $c_{d\Omega 1}$, $c_{ds\Omega 1}$ are model constants and their values are 0.005, 0.0068, 0.008, 0.004, -0.003, 0.00005, 0.00005, and 0.00025, respectively (Ali et al.[11]). c_β is the coefficient of the non-linear quadratic term and evaluated (Ali et al.[11]) as

$$c_\beta = c_{\beta 0} \frac{1}{1 + m_{ds} S^2 + m_{d\Omega} \Omega^2} \tag{16}$$

where $c_{\beta 0}$ (C_{10}, C_{20}, C_{30}) is the model constant for c_β. m_{ds} and $m_{d\Omega}$ are model constants for c_β and are of 0.01 and 0.003, respectively.

The fourth term at the right-hand side of Eq. (7) represents the effect of anisotropy in an equilibrium state. This term is first introduced by Kimura et al.[9] with coefficients C_{ij} evaluated as follows

$$C_{xx} = 2.07 (C_{30} - 2C_{10}) / 3 \tag{17a}$$

$$C_{yy} = 2.07 (C_{10} + C_{30}) / 3 \tag{17b}$$

$$C_{xy} = 0 \tag{17c}$$

$$C_{10} = 0.40, C_{20} = 0, C_{30} = -0.13 \tag{18}$$

2.2 Secondary current model

The additional terms expressing effects of secondary currents, $\hat{S}_{cx}$ and $\hat{S}_{cy}$, in Eq. (2) and Eq. (3) are defined as

$$\begin{aligned} \hat{S}_{cx} &= C_{sn} \left[\frac{\partial \bar{u}_s A_n h \sin 2\theta}{\partial x} - \frac{\partial \bar{u}_s A_n h \cos 2\theta}{\partial y} \right] \\ &+ C_{n2} \left[-\frac{\partial A_n^2 h \sin^2 \theta}{\partial x} + \frac{\partial A_n^2 h \cos \theta \sin \theta}{\partial y} \right] \end{aligned} \tag{19}$$

$$\begin{aligned} \hat{S}_{cy} &= C_{sn} \left[\frac{\partial \bar{u}_s A_n h \cos 2\theta}{\partial x} - \frac{\partial \bar{u}_s A_n h \sin 2\theta}{\partial y} \right] \\ &+ C_{n2} \left[\frac{\partial A_n^2 h \sin \theta \cos \theta}{\partial x} - \frac{\partial A_n^2 h \cos^2 \theta}{\partial y} \right] \end{aligned} \tag{20}$$

Here, C_{sn} and C_{n2} are model coefficients defined by Eq. (21) using the similarity functions of velocity profile in the longitudinal and transverse directions f_s and f_n, respectively as

$$C_{sn} = \int_0^1 f_s(\zeta) f_n(\zeta) d\zeta, \quad C_{n2} = \int_0^1 f_n(\zeta)^2 d\zeta \tag{21}$$

Hosoda et al.[5] derived the coefficients using velocity profiles proposed by Engelund[12]. $\overline{u_s}$ is depth-average velocity in the streamwise direction and is defined by Eq. (22).

$$u_s(\zeta) = \overline{u_s} f_s(\zeta) \tag{22}$$

Here, $u_s(\zeta)$ is streamwise velocity profile in the vertical direction.

The coefficient A_n means the magnitude of the secondary current and is defined as

$$u_n(\zeta) = A_n f_n(\zeta), \quad \zeta = \frac{z}{h} \tag{23}$$

Here, $u_n(\zeta)$ is transverse velocity profile in the vertical direction and z is the direction perpendicular to the bottom bed. In the model neglecting the lag between the streamline curvature and the development of the secondary current (Model 2), A_n is simply evaluated as

$$A_n = \frac{\overline{u_s} h}{R} \tag{24}$$

where R is curvature radius of the streamline. In the model proposed by Hosoda et al.[5], which includes the lag between the streamline curvature and secondary current, A_n is evaluated based on the depth-averaged transport equation of vorticity as

$$\begin{aligned} &\frac{\partial}{\partial t}\left((u_n)_s - (u_n)_b\right) + \frac{\partial}{\partial x}\left((u)_s(u_n)_s - (u)_b(u_n)_b\right) \\ &+ \frac{\partial}{\partial y}\left((v)_s(u_n)_s - (v)_b(u_n)_b\right) - \frac{1}{R}\left((u_s^2)_s - (u_s^2)_b\right) \\ &= \frac{\partial}{\partial z}\left(\frac{\tau_{zn}}{\rho}\right)_s - \frac{\partial}{\partial z}\left(\frac{\tau_{zn}}{\rho}\right)_b \end{aligned} \tag{25}$$

$$(u_n)_s - (u_n)_b = \hat{\lambda} A_n \tag{26}$$

$$\hat{\lambda} = \frac{\overline{u_s}}{\beta u_*} \frac{1}{\left(\frac{1}{3} + \beta r_*\right)^3} \left(\frac{1}{12}(\beta r_*)^2 + \frac{11}{360}(\beta r_*) + \frac{1}{504}\right) \tag{27}$$

$$r_* = \frac{\overline{u_s}}{u_*} - \frac{1}{3\beta} \tag{28}$$

Here, β is constant (=0.077) and $(u_s)_s, (u_s)_b$, $(u_n)_s, (u_n)_b$ are streamwise and transverse velocity at surface and bottom, respectively. u, v are same as ones in Eq. (2) and Eq. (3). In Model 4, which considers the change of velocity profile due to secondary current apart from the factors as the ones included in Model 3, the coefficient $\hat{\lambda}$ is derived by Onda et al.[6]. A detail description of these models is given in Hosoda et al.[5] and Onda et al.[6].

2.3 Computational scheme

The fundamental equations are solved numerically using the finite volume method with a full staggered grid including conservativeness of physical quantities and computational stability. The QUICK scheme with second order accuracy in space is employed for convective inertia terms. The Adams Bashforth method with second order accuracy in time is used for time integration.

2.4 Computational domain and conditions

The depth-averaged 2D models in the present study are applied to the open-channel confluence flow and all computations are carried out under conditions of the experiment of Weber et al.[1]. In this experiment, the channel consists of a main channel of 21.946m in length and a branch channel of 3.658 m in length located 5.486m downstream of the entrance of the main channel. Both these channels have the same width (W) of 0.914m. The total combined flow discharge (Q_t) is 0.170m^3/s and the downstream water depth is held constant at 0.296m. With these conditions, the averaged downstream velocity is 0.628 m/s corresponding to a Froude number of 0.37. A total of six runs of the experiments were conducted for six various values of q^* defined as the ratio of the upstream main channel flow (Q_m) to the total flow (Q_t).

In this study, two cases, q* = 0.25, that is, Q_m = 0.043 m^3/s and Q_b (branch discharge) = 0.127 m^3/s and q* = 0.75 (Q_m = 0.127 m^3/s and Q_b = 0.043 m^3/s), are selected for computations. Because, for the first case, q* = 0.25, this is a case which generates strong secondary current at the vicinity of the junction and is a challenge for simulating as well. The second case aims to test performance of models with condition of weak secondary current, that is, the 3D nature of the channel confluence flow diminishes greatly. In order to facilitate simulation, the length of the post-junction channel is shorten to 7W (6.398m), where the water depth is nearly constant (H_0 = 0.3054m for q* = 0.25 and H_0 = 0.3094m for q* = 0.75), while other dimensions of the computational domain are same as the ones in the experiment. Downstream bulk velocity, U_0, is approximate to 0.608 m/s for q* = 0.25 and 0.600 for q* = 0.75, respectively.

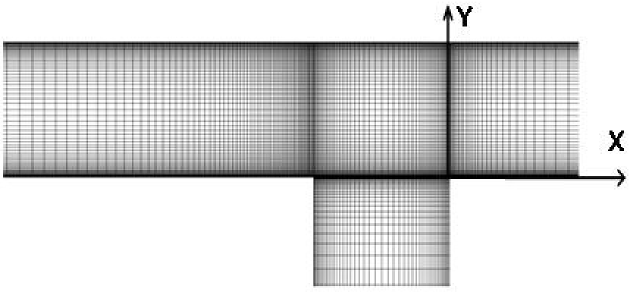

Fig.1 Computational grid around the confluence

The stretching grid is used in this study with the number of grid cells of 195 in the x-direction and 105 in the y-direction. The width of first cell near the walls is very important. Therefore, this is carefully chosen and the wall-near smallest width is selected as 0.002m (y_w/W=0.0022) in the y-direction and 0.005m (y_w/W=0.0055) in the x-direction. The computational grid around the confluence is shown in Fig. 1.

3. Results and discussions

3. 1 Selection of a turbulence model

In this study, a zero-equation turbulence model is used. Hereafter, it is called the turbulence model for simplicity. In this section, the results obtained with Model 1 using linear turbulence model (Eq.(9)) and non-linear one (Eq.(10)) for the case of q* = 0.25 are compared each other for selection of a suitable turbulence model for further computations. Fig. 2 shows dimensionless time-averaged vector field for the experimental data (Fig. 2a) and the cases using linear turbulence model (Fig. 2b) and non-linear one (Fig. 2c), respectively.

Length of separation zone is defined as the one from the downstream corner of the confluence to the reattachment point of the flow. Fig. 2a shows that the dimensionless length of separation zone is about 1.60. Model 1 with the linear turbulence model over-predicts too much length of separation zone (up to about 3.00) in comparison with the experimental results. In contrast, using the non-linear turbulence model improves much the result. However, the predicted length of recirculation region of about 1.30 with this model indicates that it under-predicts the length of this zone.

In order to explain the cause of bad prediction of the linear turbulence model above, instantaneous velocity vector fields for a short time period and depth-averaged dimensionless turbulent kinetic energy between the 300th and 450th second obtained with linear and non-linear turbulence models are displayed in Figs. 3, 4, and 5, respectively. Big differences between these two models can be realized. The linear model generates steady eddy and hardly oscillation of vortex is observed in Fig. 3, while using the non-linear one generates unsteady oscillation of vortex as obviously seen in Fig. 4. Therefore, it can concludes that not predicting the strength of vortex shedding downstream of the confluence is a main reason why Model 1 with the linear turbulence model severely over-estimates the length of the separation zone. This judgment agrees with assessment of Bosh and Rodi[13] and Kimura and Hosoda[14]. In contrast, the shedding motion is reproduced using the non-linear turbulence model, which considers effects of both strain parameter (S) and rotation one (Ω) as seen in Fig.4. Although no experimental result of vortex shedding was presented in Weber et al.[1], this computed results obtained with Model 1 using the non-linear turbulence model is sufficient to real phenomena. However, this model under-estimates the length of recirculation region. The reason, as discussed in the next section, is attributed to exclusion of effects of secondary current due to streamline curvature.

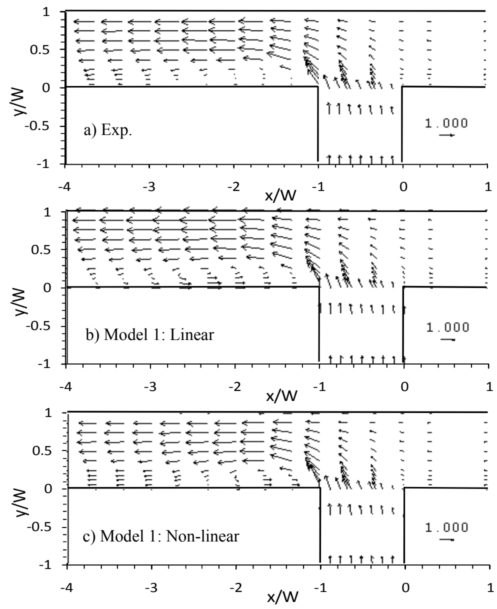

Fig. 2 Comparison of the u^*- v^* vector fields obtained with turbulence models for q* = 0.25

It can be observed from Fig. 5 that the linear turbulence model does not predict reasonably distribution of turbulent kinetic energy in downstream of the junction in comparison with the measured results. Fig. 5a shows that the most turbulent region occurs along the boundary of the passing flow and the downstream portion of the separation zone. The linear turbulence model does not reproduce this important feature. On the contrary, the non-linear turbulence model seems to predict more reasonably the distribution of turbulent kinetic energy in this region (as seen in Fig. 5c). However, it over-predicts too high turbulent magnitude. This implies a large unsteady velocity fluctuation. The reason for this limitation is unclear, but following aspects may have influences on the result. First,

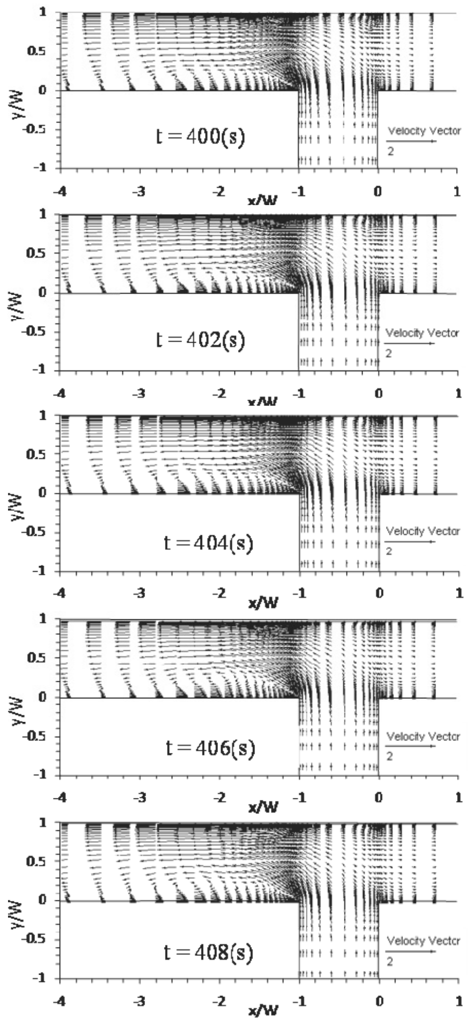

Fig. 3 Snap shot of velocity vectors computed with the linear turbulence model for q* = 0.25

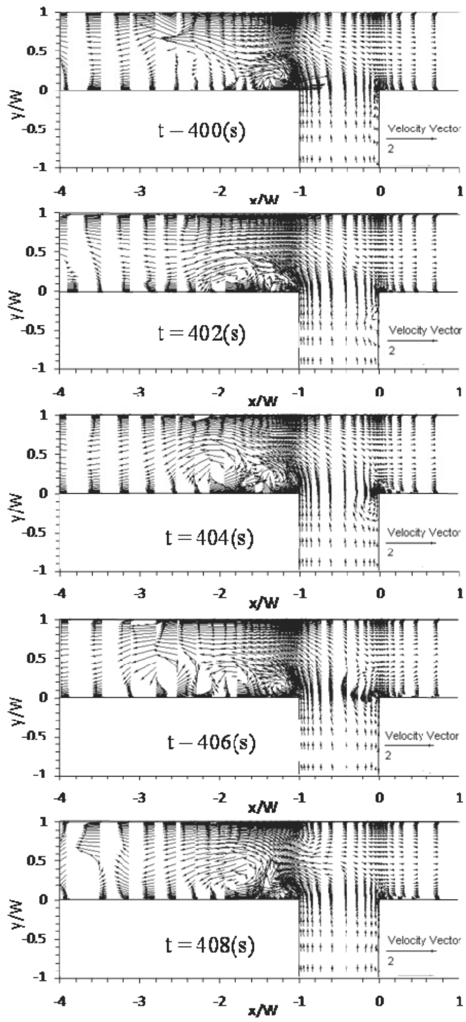

Fig. 4 Snap shot of velocity vectors computed with the non-linear turbulence model for q* = 0.25

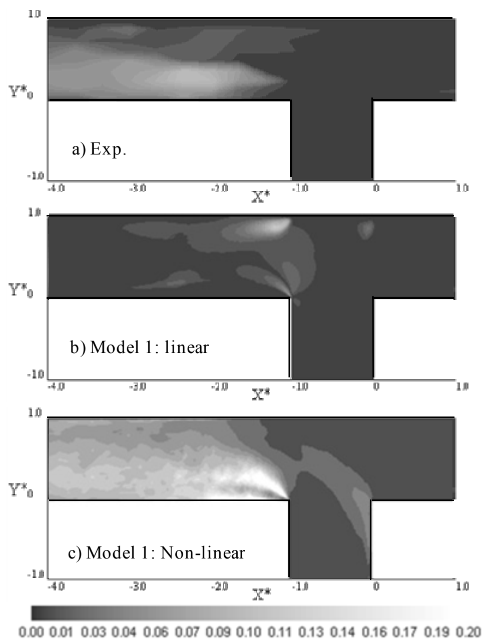

Fig. 5 Depth-averaged dimensionless turbulent kinetic energy obtained with turbulence models for q* = 0.25

Model 1 does not consider interaction between turbulence and secondary currents. Second, junction flow is highly three-dimensional and vertical velocity component is significant effects on features of flow (both primary flow and secondary ones). However, Model 1 as well as other 2D models in this study do not consider effects of vertical velocity component. Last reason may be due to unknown inherent limitations of the 2D models.

Based on the above results, the non-linear turbulence model is selected for all computations in the next sections.

3.2 u*-v* vector field and flow pattern

In this study, all distances are normalized by the channel width, named as x/W, y/W. The velocity components are normalized by the downstream average velocity, U_0, called as u^* and v^* for u/U_0 and v/U_0, respectively. The u^*-v^* vector field calculated is compared with that observed in the experiment, but some preceding manipulations are done based on the experimental data to generate a depth-averaged one. The computational results are averaged between the 300th and 450th seconds. The experimental results are shown together with the computed ones for q* = 0.25 and q* = 0.75 as seen in Figs. 6 and 7, respectively.

As seen from Figs. 6 and 7, all three models reproduce important flow patterns at the vicinity of the junction, that is, a separation zone immediately downstream of the junction and a contracted flow with higher velocity. However, it can be seen that there is a difference in separation length generated by the models for q* = 0.25 in which secondary current is strong (Fig. 6).

As indicated in the previous section, Model 1 under-predicts the length of this region (the computed length with it is about 1.30), while both Model 3 and Model 4 fairly well reproduce separation zone with its predicted non-dimensional lengths of about 1.60, which agree well with the experimental one of 1.60. It is supposed that the secondary current has an effect to extend the size of recirculation zone, because the flow near the bottom faces toward the center of this region and the reaction force acts enlarging the recirculation zone toward the outer side. Model 1 could not capture this effect because it excludes the effect of the secondary current. Hence, the separation zone produced with Model 1 should be less than those obtained using the two remaining models. This result seems to be agreeable to guess of Cheng et al.[15]. Contrarily, Model 3 and Model 4 directly consider the effects of secondary currents. Therefore, the results calculated using these models are significantly improved in comparison with that using Model 1 and well agree with the experimental one.

In contrast, no significant difference between the results generated by models is not observed for the case of q* = 0.75 in which secondary current is weak as seen in Fig. 7. The predicted separation zone lengths with three models are about 1.20, which agree well with the measured one. In this case, the 3D nature of the channel confluence flow diminishes greatly and effects of secondary current on flow in this region are not strong anymore. This is the reason why the results obtained with Models 3 and 4 are almost same as that obtained with Model 1. As known that as q* increases, the recirculation zone decreases both in width and length. This feature is very well reproduced with all three models as seen in Fig. 7 and all results in Fig. 7 are very well agreeable with the experimental one.

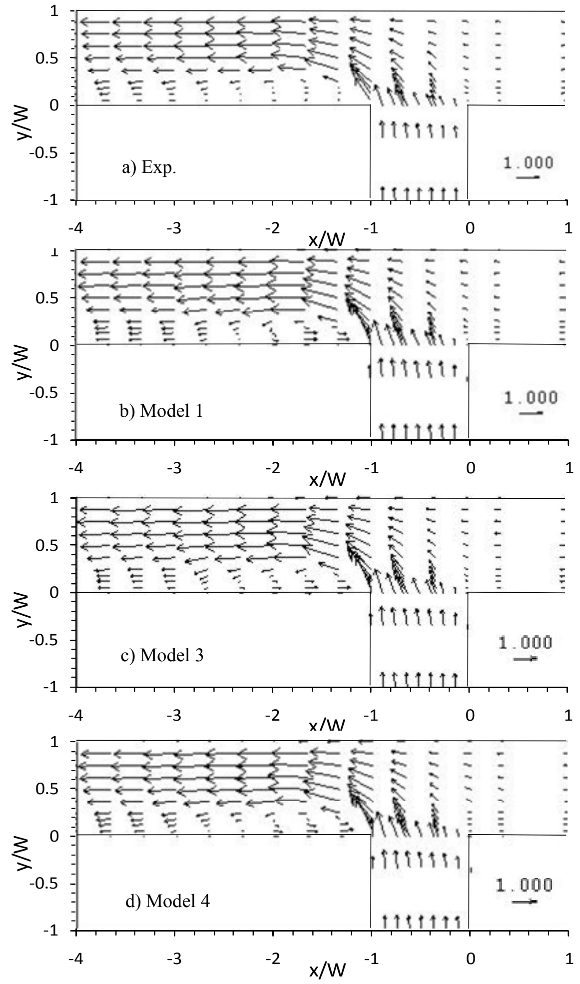

Fig. 6 Comparison of u^*-v^* vector field for q* = 0.25 with the non-linear turbulence model

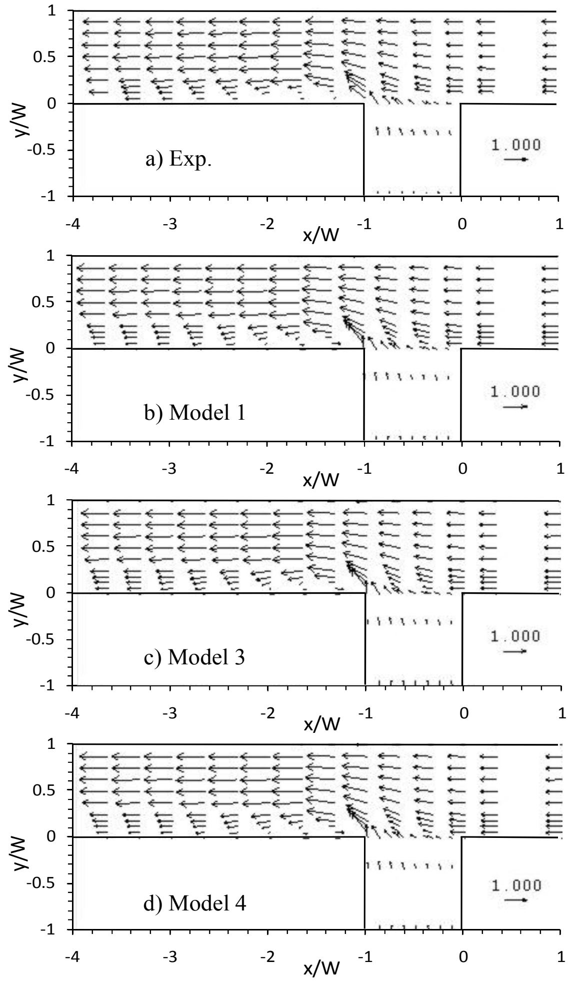

Fig. 7 Comparison of u^*-v^* vector field for q* = 0.75 with the non-linear turbulence model

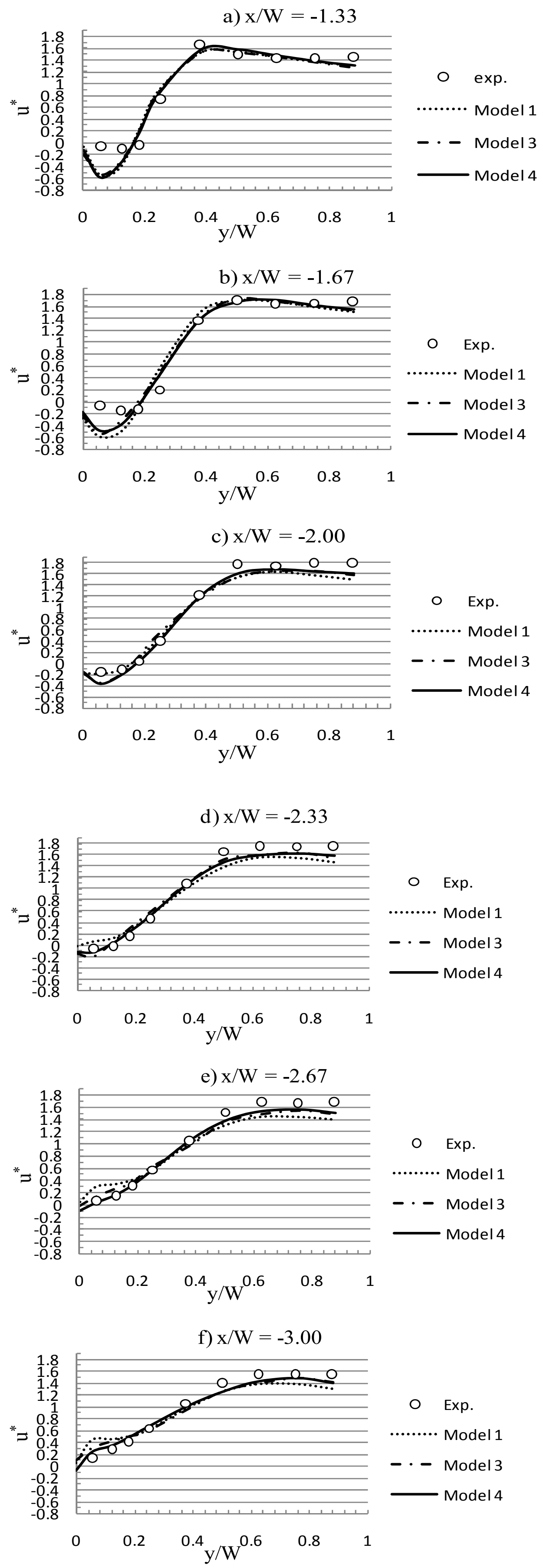

Fig. 8 Comparison of longitudinal velocity component at some locations for q* = 0.25

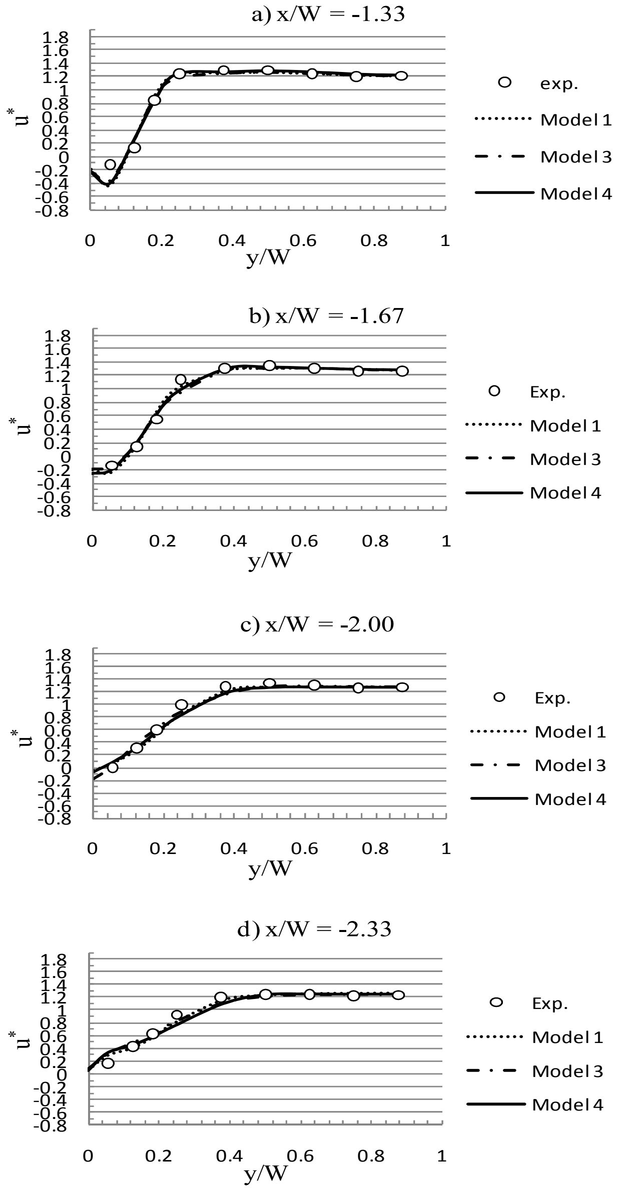

Fig. 9 Comparison of longitudinal velocity component at some locations for q* = 0.75

In addition, as partly discussed in the previous section, even though it is not presented here, an observation of process feature of the separation eddy shows that unsteady oscillation of the vortex shedding can be seen in all results generated by the three models. This characteristic is appropriate to real phenomena.

However, as also seen from Figs. 6 and 7 that all three models over-estimate velocity in the beginning part of the separation, which is adjacent to the junction. It may be because the flow in this reach is characterized with highly three dimensionality and a 2D model should not capture all flow features in spite of secondary current effects considered.

3.3 Velocity components

In order to see more detail of performance of the models, comparison of velocity profiles in the x-and y- direction is carried out. Fig. 8 shows the streamwise velocity component profiles at some cross-sections along the post-confluence main channel for q* = 0.25, while Fig. 9 depicts those at the same places for q* = 0.75 with the non-linear turbulence model. All velocity values are averaged over the depth. Positive values in Figs. 8 and 9 indicate downstream motion, while negative ones show upstream motion.

It is observed in Fig. 8 that the results obtained with Model 3 and Model 4 agree well with the experimental ones, except in the beginning reach of the separation zone (In this reach, all models over-predict velocity as mentioned above). However, the similar agreement is not obtained with Model 1, because Model 1, as mentioned above, under-predicts the length of the separation zone. This can be seen in more details here. The separation zone generated with Model 1 seems to drop somewhere before the section of x/W = -2.33, while it, in reality, extends to a place around the section of x/W=-2.67. This can be realized, because velocity direction in the region near the inner bank of the main channel changes between the section of x/W=-2.00 and the section of x/W=-2.33 and the velocity profile in this region has a tendency to be flattened in the next sections as seen in Figs. 8e and 8f. The reason for this shortcoming of Model 1, as explained above, is due to not considering adequately effects of secondary current. Unlike the case of q* = 0.25, Fig. 9 shows that there is no significant difference in velocity profiles as well as in location where the separation zone drops between the results with Model 1 and those with the two remaining ones for q* = 0.75. The reason for this, as indicated above, is that as q* is large, secondary current is weak and has not significant effects on flow. All simulated results agree very well with the experimental ones.

In addition, by more carefully observing Fig. 8, a general tendency of flow passing through the contracted region reproduced with all three models can be realized. When flow enters the contracted zone (the outer half of the main channel), its velocity increases (as seen in Figs. 8a, b) due to gradual contraction of effective section through it flow passes. Then flow velocity reaches the peak in somewhere around the sections of x/W=-2.00 (as seen in Fig. 8c) and once decreases due to enlargement of effective section (as seen in Figs. 8d, e and f). This tendency seems to quite suitable for the experimental results. The similar tendency is also recognized in Fig. 9.

One another thing is that there is an obvious difference in longitudinal velocity profiles between the cases of small q* (=0.25) and large q* (=0.75). Fig. 8 shows that the part with high velocity skews toward the outer half of the main channel, while Fig. 9 indicates that this part occupies not only the outer half but also a portion of the inner one of the main channel with less velocity than that for q* = 0.25. The reason is that the separation region for small q* is greater than that for large q* as seen in Figs. 6 and 7. This causes a smaller contracted flow region with higher velocity for small q* in comparison with that with lower velocity for large q*.

It is also seen that it is not clear to realize difference between the results obtained using Model 3 and Model 4 with a comparison of depth-averaged velocity components. This may be because secondary current has a stronger effect on vertical mainstream velocity profile than on depth-averaged mainstream velocity one.

In summary, for confluence flow with predominant discharge coming from the lateral channel (small q*), Model 3 and Model 4 are superiority ones over Model 1. In the case of almost confluence flow coming from the main channel (large q*), all the models presented well reproduce flow pattern at the vicinity of a confluence channel.

3.4 Velocity profiles

To highlight superiority of Model 3 and Model 4 over Model 1, secondary current pattern is reproduced with these models. In order to do this, first, water depth is split into layers (21 layers in the present study). Then, the vertical velocity component (named as w) is estimated with help of the continuity equation written for the 3D and the 2D velocity results obtained above as well as using the similarity functions of velocity profile in the longitudinal and transverse directions, f_s and f_n, respectively. Fig. 10 shows the v*-w* velocity field obtained with this approach (with w* is the dimensionless vertical velocity component defined as w/W) for present computation and experimental data at the cross-section x* = 1.67 for q* = 0.25. It can be seen that the secondary flow can been generated with Model 3 and Model 4. Both the experiment and the numerical model show that the secondary flow moves toward the right bank near the surface and to the left bank near the bed when looking downstream, thus creates a large clockwise vortex. However, both the two models presented do not well reproduce the position of this vortex and under-predict the strength of this vortex. Model 3 generates the vortex with its center skewing toward the inner half of the channel. Hence, velocity magnitude in the outer half of the channel is weak. Model 4 with considering the change of streamwise velocity induced by secondary currents significantly improves the position of vortex with its center locating in the middle area of the channel. This increases velocity magnitude in the outer half of the channel, especially in the near wall region. In addition, it can be seen that in the separation zone, which is near the inner bank, the experimental data shows that there is another small vortex rotating in the same direction as that of the large vortex. However, Figs. 10b and 10c show that there is also another small vortex in this zone, but it rotates in the reverse direction, anti-clockwise one. The reason for that can be explained as follows. Computation of the vertical streamwise and transverse velocity distributions is based on depth-averaged streamlines. This implies that there is no change of streamline direction in the flow layers. Hence, this leads to not predicting shape change of the separation zone in the vertical direction, that is, size of this region is same along the water depth. The near bed flow, which moves toward the inner bank, is prevented from approaching the wall and hits the separation zone border, thus deflects upward. When this vertical flow reaches the surface, it deflects toward both the inside and outside due to the weight of the water itself. This process continues and creates an anti-clockwise vortex in the separation zone. The shear border area between the recirculation region and the contracted one seems to like a vertical axis controlling the two vortices. In Fig. 10b, the strength of the vortex generated with Model 3 is greater than that with Model 4 in Fig. 10c. Therefore, the center of the larger vortex with Model 3 is closer to this axis than that with Model 4.

As seen from Figs. 10b and 10c that the strength of secondary current with Model 3 is stronger than that with Model 4. This difference can be expected, because Model 4 predicts a deceleration of streamwise velocity in the surface flow layer and an acceleration of this velocity component in the bottom one, which Model 3 does not. These seem to lead to a decrease in strength of vorticity predicted by Model 4 in comparison with that obtained by Model 3.

In comparison with the experimental data (Fig. 10a), it can be realized that Model 4 predicts secondary flow better than does Model 3. Fig. 9 also shows that the presented models do not predict precisely secondary current patterns. However, the streamwise velocity is reproduced reasonably as shown in Figs. 6 and 9. This can be explained as follows. In Model 3, similarity velocity functions are the ones derived by Engelund (1974), which consider vertical velocity profiles as functions of friction factors only. However, in Model 4, besides friction factors, an important feedback mechanism between the main and secondary flow is included. The important role it plays is that it reduces imbalance between the centrifugal force and the transversal pressure gradient, which is known to produce secondary current in curved flow, thus it causes decreasing secondary current intensity. Difference in the approach of evaluation of velocity similarity functions may have a stronger effect on the vertical velocity profiles than on the horizontal depth-averaged ones. The above aspects may make good prediction of streamwise velocity with both the models. However, in their results, there are still some points those do not agree with the experimental data. The reason for that is still not clear. However, the following aspects may influence on the prediction of secondary current pattern in the present study:

(1) The models presented do not predict change in streamline direction at a location in the visualized flow layers. This causes an under-estimation of size of the separation zone at the near surface area, thus an over-prediction of size of the contracted flow one and an over-prediction of that at the near bed region, thus an under-estimation of size of the contracted flow one;

(2) At the vicinity of a confluence channel flow, vertical velocity gradient is also a significant aspect; however, this is not considered by the 2D models presented in this study;

(3) The models presented only include effects of secondary currents induced by streamline curvature, but exclude effects of horizontal vortex, which is formed due to downstream deflection of the lateral flow entering the confluence and impinging on the main channel flow; and

(4) When the lateral flow impinges on the main one at the junction region, a part of its surface water is defected downward. This motion creates a secondary current, which has not been defined so far. However, this flow pattern is not included in the present study. Further study for this kind of secondary current is necessary, and a 3D simulation is able to accomplish this task.

3.5 Water surface elevation

In this section, the results of water surface elevation, which is normalized by the channel width (W), predicted with the models are compared to the experimental one. Figs. 11 and 12 show the contours of measured and predicted dimensionless water surface elevations by the experiment of Weber et al.[1] and by using Models 1, 3 and 4 for q* = 0.25 and q* = 0.75, respectively. As known, one of distinctive characteristics of a sharp-edged, open-channel junction flow is an increase in depth from the downstream channel to the upstream contributing channels. This important feature is captured in all predicted results of water surface elevation using the models for both the cases of q* = 0.25 and q* = 0.75 (as seen in Figs. 11 and 12). One another important feature is that the water surface depression within the

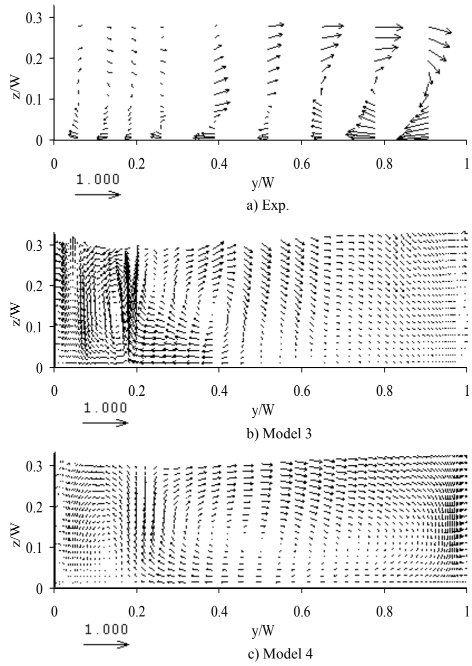

Fig. 10 Cross-section view of vector field for q* = 0.25

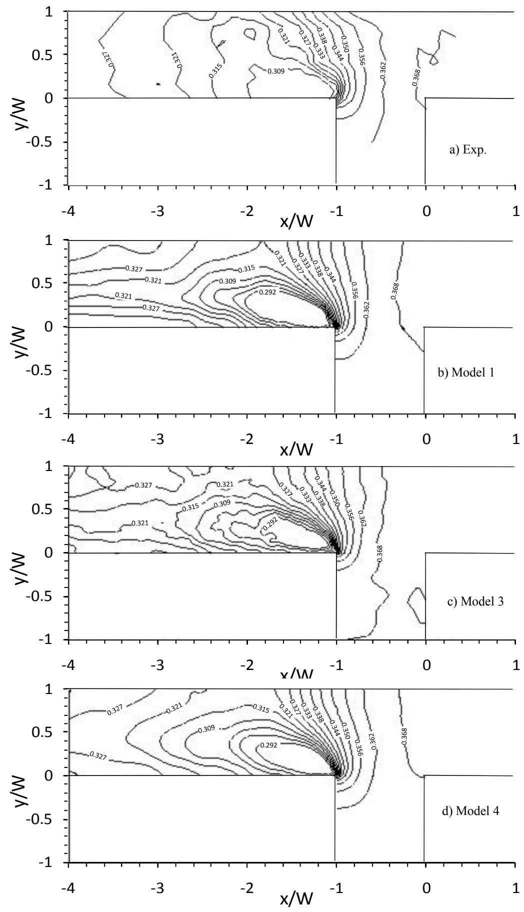

Fig. 11 Comparison of water surface mappings for q* = 0.25

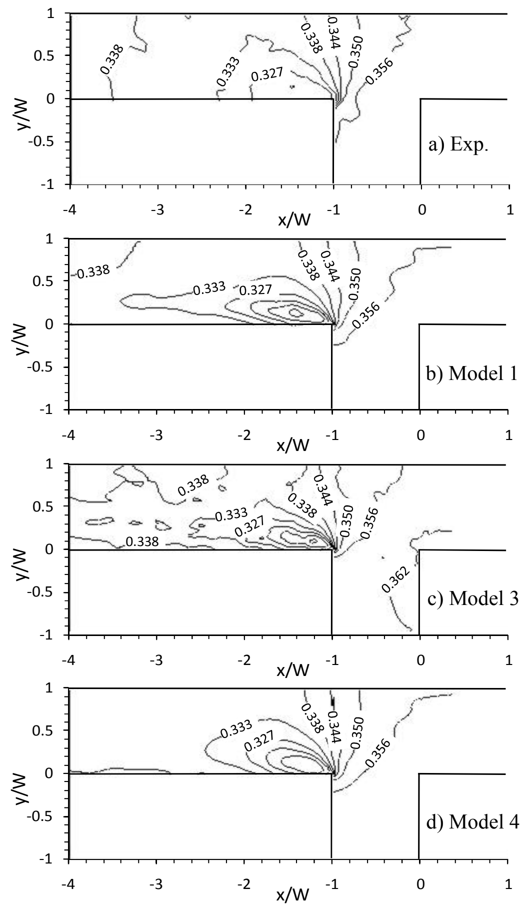

Fig. 12 Comparison of water surface mappings for q* = 0.75

separation, adjacent and downstream of the branch as q* is low, is deeper and more extensive than that as q* is high. This characteristic is also well captured with the models. Moreover, it can be seen that Model 1 and Model 4 predict well water surface elevations in the region where flow enters the contracted zone and its upstream region, while Model 3 over-predicts slightly water surface elevation in these zones. The reason may be because Model 3 results in a slightly larger contraction than that with Models 4 and 1 leading to an slight increase in water depth upstream of this region.

Model 4 seems to perform a solution closer to the experimental data in comparison with the two remaining models for both q* = 0.25 and q* = 0.75. However, it can be seen that all three models under-predict water surface elevation within the separation, adjacent and downstream of the lateral branch as well as downstream of the separation zone.

With this comparison, it seems that difference between the models with (Model 4) and without (Model 3) consideration of change of mainstream velocity profile due to secondary current is more obvious than that with the comparison of depth-averaged velocity profiles in the previous section. Water surface profiles across the contracted flow region and upstream of this section obtained with Model 3 have the slightly higher peaks as realized via higher contours in the outer half of the main channel than those obtained with Model 4 as seen in Figs. 11c, 11d, 12c and 12d. As known that, secondary current in the curved flow is produced due to an imbalance between the centrifugal force and the transversal pressure gradient. Moreover, the feedback between the main and secondary flow plays an important role, because it reduces this imbalance, and thus secondary current intensity. However, this important feedback mechanism is not included in the linear models (not the linear turbulence model mentioned in the previous sections) in which the velocity distribution in streamwise direction is assumed to be uniform. Therefore, these models fail to represent curved flow and over-estimate the momentum transport as well as secondary current intensity as pointed out by Blankaert[16]. Model 3, which is proposed by Hosoda et al.[5], is also such a linear model, because it evaluates the momentum transport based on the model developed by Engeland[10] in which the uniform velocity distribution in mainstream direction is assumed. Therefore, Model 3 over-predicts secondary current. This also means that centrifugal force is over-estimated and this may be a reason why water surface profiles across the contracted section obtained with Model 3 are slightly higher in the outer half of the main channel than those obtained with Model 4. This difference is more obviously realized in Fig. 11. However, causes of this difference may be also related to aspects mentioned in Section 3.4 above.

4. Conclusion

In this study, four different types of depth-averaged 2D models with and without considering secondary currents are applied to open-channel confluence flow. The calculated results allow us conclude that as the ratio of the upstream main channel flow to the total flow (q*) is high, all three models presented perform well most distinctive features of a sharp-edge open-channel junction. However as q* is low, the models with effects of secondary current (Models 3 and 4) are superiority ones over the model without these effects (Model 1) except over-predicting streamwise velocity component in the upstream part of the separation zone and under-predicting water surface elevation within, adjacent and downstream of the separation region. Model 2, which considers effects of secondary current without lag between the streamline curvature and development of secondary currents, fails to apply to flow conditions presented in this study for both low q* and high q*. This indicates high applicability of the depth-averaged 2D models with effect of secondary current (Model 3 and Model 4) to an open-channel junction flow as well as demonstrates failure of Model 2, in application to sharp-edged, open-channel junction.

References

1) Weber, L. J., Eric, D. S., and Nicola, M., Experiments on flow at a 90^o open-channel junction, *J. Hydr. Eng.,* Vol.127(5), 340-350, 2001.
2) Huang, J., Weber, L. J., and Lai, Y. G., Three-dimensional numerical study of flows in open-channel junctions, *J. Hydr. Eng.,* Vol. 128(3), 268-280, 2002.
3) Quing-Yuan, Y., Xian-Ye, W., Wei-Zhen, L., and Xie-Kang, W., Experimental study on characteristics of separation zone in confluence zones in rivers, *J. Hydr. Eng.*, Vol. 14(2), 166-171, 2009.
4) Kalkwijk, J. P. and De Vriend, H. J., Computational of the flow in shallow river bends, *J. Hydr. Re.*, IAHR, Vol.18(4), 327-342, 1980.
5) Hosoda, T., Nagata, N., Kimura, I., Michibata, K., and Iwata, M., A depth-averaged model of open channel flows with lag between main flows and secondary currents in a generalized curvilinear coordinate system, *Advances in Fluid Modeling & Turbulence Measurements*, (eds. H. Ninokata, A Wada and N. Tanaka), World Scientific, 63-70, 2001.
6) Onda, S., Hosoda, T., and Kimura, I., Refinement of a depth-averaged model in curved channel in generalized curvilinear coordinate system and its verification, *Ann. J. Hydr. Engrg, JSCE,* Vol.50, 769–774, 2006.
7) Kimura, I., Hosoda, T., and Onda, S., Fundamental properties of suspended sediment transport in open channel flows with a side cavity, *Proceedings of RCEM 2007*, Enschede, Netherlands, Balkema Publishers, 1203-1210, 2007.
8) Kimura, I., Onda, S., Hosoda, T., Shimizu, Y., and Hagiwara, K., Computations of suspended sediment transport in meandering channels using depth-averaged models with effects of secondary currents, *Proceedings of RCEM 2009*, Santa Fe, Agentina, Balkema Pblishers, 619-626, 2009.
9) Kimura, I., Uijttewaal, W. S. J., Hosoda, T., and Ali, M. S., URANS Computations of shallow grid turbulence, *J. Hydr. Eng.*, Vol.135(2), 118-131, 2009.
10) Nezu, I. and Nakagawa, H., Turbulence in open-channel flows, *IAHR Monograph*, Balkema, Rotterdam, Netherlands, 1993.
11) Ali, M. S., Hosoda, T., and Kimura, I., A non-linear k-ε model to predict the spatial change of turbulence structures in large scale vortices, *Journal of Applied Mechanics*, JSCE, Vol.10, 723-732, 2007.
12) Engelund, F., Flow and bed topography in channel bends, *Proc, ASCE, J. Hydr. Div.*, Vol.100, HY11, 1631-1648, 1974.
13) Bosh, G. and Rodi, W., Simulation of vortext shedding past a square cylinder with different turbulence models, *International Journal for Numerical Methods in Fluids* **28,** 601-616, 1998.
14) Kimura, I. and Hosoda, T., A non-linear k-ε model with realizability for prediction of flows around bluff bodies, *International Journal for Numerical Methods in Fluids* 42**,** 813-837, 2003.
15) Cheng, L., Komura, S., and Fujita, I., Numerical simulation of the confluence flow by using k-ε models, *Ann. J. Hydr. Engrg, JSCE*, Vol.36, 169–174, 1992.
16) Blankaert, K., Flow and turbulence in sharp open-channel bends, PhD-thesis, Ecole Polytechnique Federale de Lausanne, 2002.

(Received: March 9, 2010)